

Buckling vs unilateral constraint for a multistable metamaterial element

N. HIMA^{A,B}, D. BIGONI^A AND F. DAL CORSO^{A,1}

^A*DICAM, University of Trento, via Mesiano 77, I-38123 Trento, Italy.*

^B*FIP MEC srl, via Scapacchiò 41, 35030 Selvazzano Dentro PD, Italy.*

Abstract

A structural element is designed and investigated, forming the basis for the development of an elastic multistable metamaterial. The leitmotif of the structural design is the implementation of a strut characterized by a bifurcation occurring at either vanishing tensile or compressive load. It is shown that buckling at null load leads to a mechanical equivalence with a unilateral constraint formulation, introducing shocks in dynamics. Towards a future analysis of the latter, the nonlinear quasi-static response is investigated, showing the multistable character of the structure, which may appear as bistable or tetrastable.

Keywords: Buckling, unilateral constraint, nonlinear motion, vibration control, metamaterials.

1 Introduction

Elastic metamaterials represent a blowing-up research field, finding crucial applications in vibration control, wave filtering and conditioning [1, 2, 3, 4, 5, 6, 7, 8, 9, 10, 11, 12, 13, 14, 15, 16, 17, 18]. However, meta-materials exhibit extraordinary mechanical properties even when subject to quasi-static loading, particularly when large deformations are involved [19, 20, 21, 22, 23, 24, 25, 26]. Examples are numerous, including cloaking [27], extreme stiffness [28], shape morphing [29], auxeticity [30, 31], negative thermal expansion [32], and multistable architectures [33, 34, 35, 36, 37]. A flow in this research stream is the exploitation of structures beyond buckling and instability loads [38], in a range of extreme deformations [39]. Under these conditions, structures become ‘elastic machines’, capable of realizing soft actuation [40], or developing propulsion forces [41, 42], or being used as soft devices [43].

The nonlinear analysis of the structure shown in Fig. 1(a), forming an element to be exploited in a metamaterial design (Fig. 1(d)), is the subject of the present article. The structure is composed of two superimposed layers of rigid bars essentially working as quadrilateral linkages, but equipped with an elastic hinge and with a bar containing a slider (a constraint allowing only relative transverse displacement between the connected elements [44]) which buckles under tensile load of vanishing magnitude.

The latter structural element provides the key mechanical feature implemented in the design of a simple structure, which displays a series of remarkable mechanical features, although characterized by

¹Corresponding author: Francesco Dal Corso (francesco.dalcorso@unitn.it)

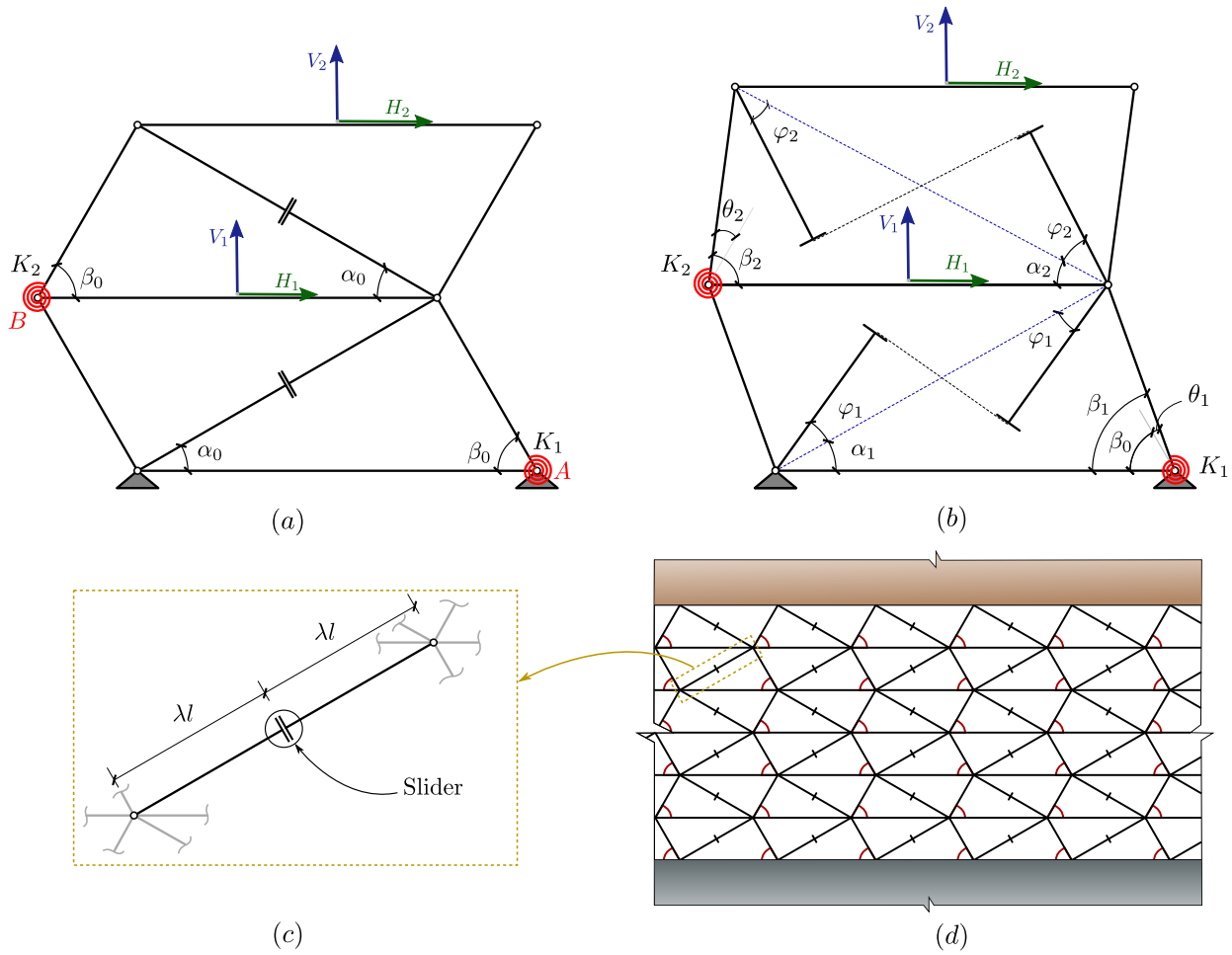


Figure 1: The unit structure of the proposed multistable metamaterial element (sketched in the inset (d)). It is made up of two superimposed articulated quadrilateral structures, both composed of rigid bars and containing an elastic hinge (of stiffness K_j , $j = 1, 2$) and a slider at the midpoint of one of the inclined rigid bars. The introduction of the slider (c) provides the key mechanical feature, because it buckles at null axial force, realizing a unilateral constraint in compression. (a) Undeformed and (b) deformed configuration of the two-layer structure subject to dead loads H_j and V_j , described through the misalignment angles φ_j or equivalently through the difference angles θ_j .

only two degrees of freedom. These are related to the fact that the two structural layers can behave independently or synergically and involve a purely geometrical nonlinearity. In particular, the following features are found: (i.) the critical loads for bifurcation depend on the geometry of the structure only through the angle β_0 , but are independent of the angle α_0 and of the hinge stiffness K_j ($j = 1, 2$); (ii.) the structure can have multiple stable equilibrium configurations under the same applied loads, which may be displayed as *bistable* or *tetrastable* (as shown in Fig. 2); (iii.) the applied loads can be varied in a way that a negative (a positive) slope in the load/displacement curve represents a stable (an unstable) loading path. Most of these features are related to the presence of an element bifurcating in tension. However, it is shown that the a structure exhibiting exactly the same mechanical behaviour can be obtained through a proper modification of the quadrilateral linkages and substitution of the slider with a hinge, so that the inclined structural element suffers a bifurcation at a vanishing compressive load. Interestingly, the elements buckling at vanishing force can be replaced by unilateral constraints, which

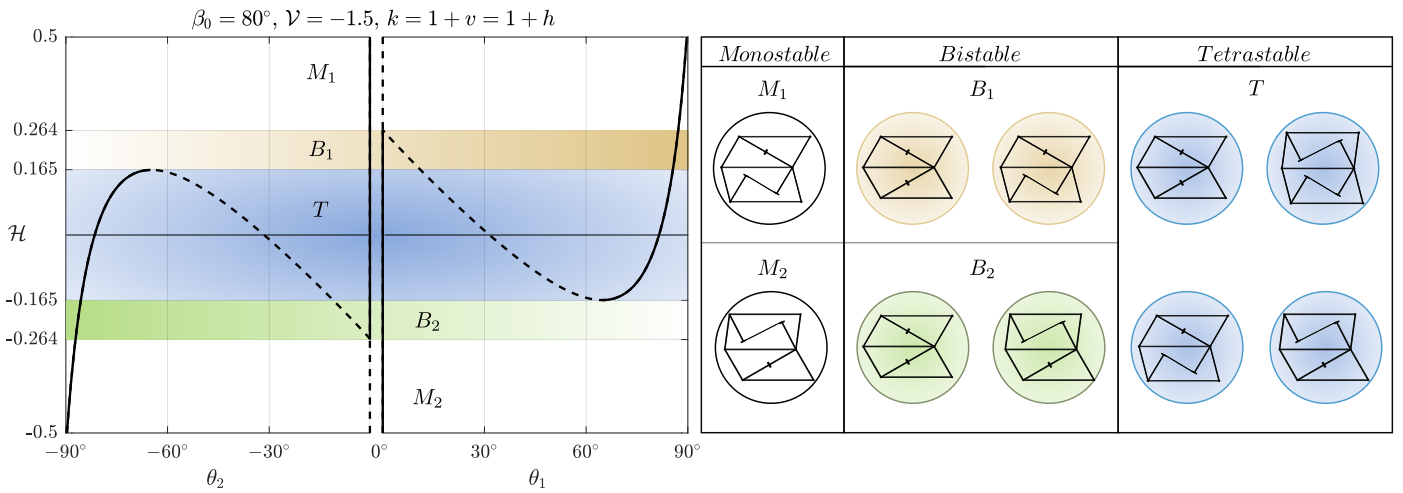


Figure 2: Equilibrium diagram for the structure shown in Fig. 1(a) and (b), when subject to a constant vertical load \mathcal{V} , expressed in terms of the difference angles θ_1 and θ_2 as functions of the variable horizontal load \mathcal{H} . Stable and unstable configurations are displayed as continuous and dashed curves, respectively. By varying the horizontal load \mathcal{H} , the system displays monostability (M_1 and M_2), bistability (B_1 and B_2), and tetrastability (T), through the corresponding deformed configurations sketched beside.

produce the same effect on the structure, but eliminates the bifurcation. This important aspect (to which the next Section is dedicated) implies that the dynamic behaviour of the structure is characterized by the occurrence of impacts, a topic that will be analyzed elsewhere.

2 Buckling vs unilateral constraint

The elementary triangular structure reported in Fig. 3(a) represents the essential building block of the two-layer unit structure depicted in Fig. 1(a), which in turn forms the structure leading to the interface shown in Fig. 1(d). Although the rigid bar containing a slider at the mid-span is at equilibrium in its straight configuration when axially loaded, bifurcation occurs at null axial force. Therefore, this single structural element displays an infinite stiffness under compression and a null stiffness under tension. As a consequence, the mechanical behaviour of the rigid bar containing the slider becomes equivalent to a unilateral constraint, providing support only when compressed. This equivalence occurs only from the mechanical point of view, but not from a purely mathematical perspective. Indeed, the structure shown in Fig. 3(c) is subject to a bifurcation, while that reported in Fig. 3(b) is not. This crucial point is now explained in detail.

For the structure in Fig. 3(a), the total potential energy Π can be written as the difference between the strain energy stored in the rotational spring of stiffness K and the work done by the external dead loads (H and V)

$$\Pi(\theta) = \frac{K\theta^2}{2} - Hl [\cos \beta_0 - \cos(\beta_0 + \theta)] - Vl [\sin(\beta_0 + \theta) - \sin \beta_0], \quad (1)$$

where l is the length of the bar inclined at an angle β_0 in the undeformed configuration, with the latter subject to the following geometrical constraint

$$0 < \beta_0 < \pi, \quad (2)$$

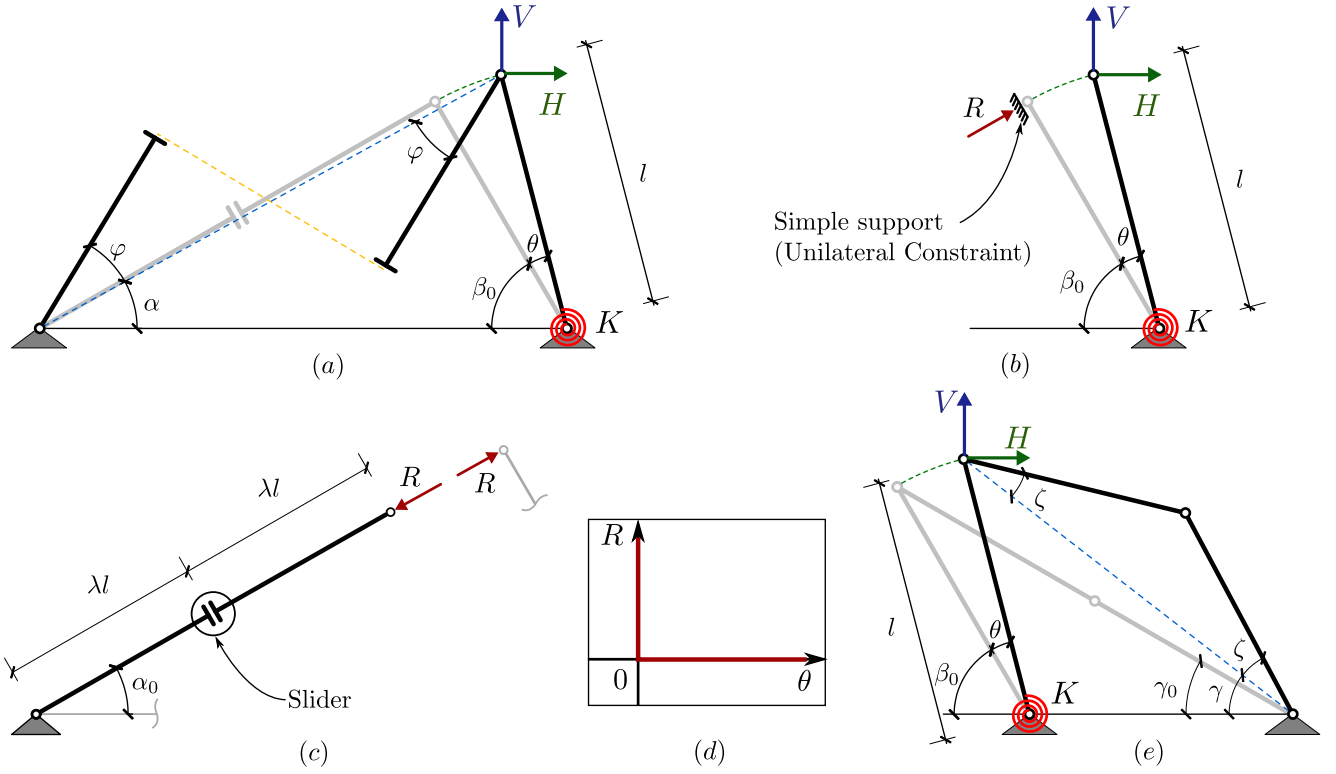


Figure 3: (a) The essential building block (forming the two-layer unit structure shown in Fig. 1a) is characterized by one elastic hinge of stiffness K and is loaded with vertical V and horizontal H dead forces. The two structural elements, sketched in isolation in parts (b) and (c), are able to sustain an arbitrary amount of compression R , but they cannot bear any tensile load, as one is equipped with a unilateral constraint and the other immediately buckles in tension (because it contains a slider). Note that bifurcation does not play any role for unilateral contact (b), described by (d) the Signorini diagram. (e) A quadrilateral linkage with two bars aligned parallel buckles in compression at null load, realizing an unilateral kinematics equivalent to the elementary structure (a).

while the difference angle θ is the Lagrangian parameter subject to the unilateral constraint $\theta \geq 0$ and defining the inclination $\beta_0 + \theta$ in the deformed configuration. Considering now the system in Fig. 3(b), equivalent to the former one, the total potential energy Π can be written as a function of another Lagrangian parameter, the misalignment angle φ of the rigid bar with slider, as

$$\Pi(\varphi) = \Pi(\theta(\varphi)), \quad (3)$$

where the difference angle θ is defined in relation of the misalignment angle φ as

$$\theta(\varphi) = \arccos(\cos \beta_0 - \psi \tan^2 \varphi) - \beta_0, \quad (4)$$

a relation that cannot be inverted, as θ is insensitive to the sign of φ , $\theta(\varphi) = \theta(-\varphi)$, and with ψ defined as

$$\psi = \frac{\sin \beta_0^2}{2 \sin \alpha_0 \sin(\alpha_0 + \beta_0)}. \quad (5)$$

Note that a Taylor series expansion of eq. (4) about $\varphi = 0$ truncated at the second-order leads to

$$\theta(\varphi) \approx \frac{\psi}{\sin \beta_0} \varphi^2, \quad (6)$$

highlighting the property that the two angle measures at small amplitude have different order. This last property implies that θ cannot be used as a Lagrangian parameter for the structure in Fig. 1(c) and (d).

Equilibrium of the structure sketched in Fig. 3(a) corresponds to the stationary condition for the total potential energy $\Pi(\varphi)$, which through the chain rule of differentiation becomes

$$\frac{\partial \Pi(\theta)}{\partial \theta} \frac{\partial \theta}{\partial \varphi} = 0, \quad (7)$$

equivalent to

$$\frac{\partial \Pi(\theta)}{\partial \theta} = 0, \quad \text{and/or} \quad \frac{\partial \theta}{\partial \varphi} = 0. \quad (8)$$

Note that the second condition in eq. (8) becomes possible only when the order of magnitude in the relation between the parameters is different, as for the present structure as shown by (6).

From eq. (1) the condition

$$\frac{\partial \Pi(\theta)}{\partial \theta} = K\theta - l[H \sin(\beta_0 + \theta) + V \cos(\beta_0 + \theta)], \quad (9)$$

follows, while from eq. (4) the derivative of θ with respect to ϕ can be written as

$$\frac{\partial \theta}{\partial \varphi} = \frac{2 \psi \tan \varphi}{\cos^2 \varphi \sqrt{1 - (\cos \beta_0 - \psi \tan^2 \varphi)^2}}. \quad (10)$$

Expansions truncated at the second-order of the two above derivatives at small values of φ provide

$$\left. \frac{\partial \Pi(\theta)}{\partial \theta} \right|_{\theta(\varphi)} = -l(H \sin \beta_0 + V \cos \beta_0), \quad \frac{\partial \theta}{\partial \varphi} = \frac{2 \psi}{\sin \beta_0} \varphi, \quad (11)$$

showing that the equilibrium is not only attained for the trivial configuration for every load combination

$$\varphi = \theta = 0 \Rightarrow \frac{\partial \theta}{\partial \varphi} = 0 \Rightarrow \frac{\partial \Pi}{\partial \varphi} = 0 \quad \forall V \text{ and } H, \quad (12)$$

but also for non-trivial configurations at the bifurcation condition

$$H \sin \beta_0 + V \cos \beta_0 = 0 \Rightarrow \frac{\partial \Pi(\theta)}{\partial \theta} = 0 \Rightarrow \frac{\partial \Pi}{\partial \varphi} = 0 \quad \forall \varphi \neq 0 \text{ (with } \varphi^2 \ll \varphi). \quad (13)$$

Stability of the trivial configuration can be analyzed by considering the sign of the second derivative of $\Pi(\varphi)$, calculated at $\varphi = 0$ as

$$\left. \frac{\partial^2 \Pi(\varphi)}{\partial \varphi^2} \right|_{\varphi=0} = -\frac{l \sin \beta_0}{\sin \alpha_0 \sin(\alpha_0 + \beta_0)} (H \sin \beta_0 + V \cos \beta_0). \quad (14)$$

Considering that

$$\alpha_0 > 0, \quad \alpha_0 + \beta_0 < \pi, \quad (15)$$

eq. (14) shows that the trivial configuration is stable whenever

$$H \sin \beta_0 + V \cos \beta_0 < 0, \quad (16)$$

and otherwise is unstable. Therefore, the structural element containing the slider, Fig. 3(c), essentially works as that subject to the unilateral constraint, Fig. 3(b), because it buckles at null axial force and does not bear any tensile load.

The equilibrium equation for the structure subject to the unilateral constraint, Fig. 3(b), is given by

$$\frac{\partial \Pi(\theta)}{\partial \theta} \delta \theta \geq 0, \quad (17)$$

for all virtual displacements $\delta \theta \geq 0$, so that the unilateral Kuhn-Tucker conditions are satisfied

$$\theta \geq 0, \quad R \geq 0, \quad \theta R = 0, \quad (18)$$

where R is the reaction of the unilateral support. Equation (17) holds with the ‘=’ sign for all $\theta > 0$ and becomes equivalent to eq. (16), except that ‘<’ has to be replaced with ‘=’. Therefore, *the presence of the unilateral constraint eliminates the bifurcation*, so that the buckling analysis is turned into a purely equilibrium problem. The unilateral constraint is smooth, so that it does not alter the conservativeness of the system (which is subject to dead loading in the present formulation). For this reason, the Dirichlet stability theorem applies even in the boundary case $\theta = 0$. There, the total potential energy is allowed to possess a non-analytical minimum to verify stability. Therefore, positiveness of the first derivative of eq. (1), eq. (9) evaluated at $\theta = 0$, leads exactly to the same condition as in eq. (16), thus confirming that both structures shown in Fig. 3(a) and (b) exhibit the same mechanical behaviour. Note that for simplicity, the term *bifurcation* will be associated in the following to both the misalignment and difference angles, φ and θ .

Buckling in tension vs compression. The kinematics of the inclined bar of length l described by $\theta > 0$ has been considered as the result of tensile buckling in the simple triangular structure in Fig. 3(a). The same kinematics for the inclined bar of length l can be, however, equivalently achieved through buckling in compression as for the elementary triangular structure in Fig. 3(e), now incorporating a bar with a hinge (instead of a slider), initially straight and inclined at γ_0 in the undeformed state. In this latter structure, the difference angle θ becomes the following function of the misalignment angle ζ

$$\theta(\zeta) = \arccos \left[\frac{(\cos^2 \zeta - \cos^2 \gamma_0) \sin^2 \beta_0}{2 \sin \gamma_0 \sin(\beta_0 - \gamma_0)} + \frac{\sin(2\beta_0) \cos \gamma_0 - (\cos^2 \beta_0 + 1) \sin \gamma_0}{2 \sin(\beta_0 - \gamma_0)} \right] - \beta_0, \quad (19)$$

whose expansion for small values of ζ simplifies to

$$\theta(\zeta) \approx \frac{\sin \beta_0}{2 \sin \gamma_0 \sin(\beta_0 - \gamma_0)} \zeta^2, \quad (20)$$

showing the different order in the difference θ and misalignment ζ angles, in analogy to the misalignment angle φ in the triangular structure with tensile buckling, eq. (6).

Since the total potential energy $\Pi(\theta)$ (1) is the same for the two triangular structures shown in Figs. 3(a) and (e) when the inclined bar is subject to the same rotation $\theta(\varphi) = \theta(\zeta)$, the two structures, although based on two different types of buckling, are mechanically equivalent. For this reason, the results presented in the following and obtained for the system composed of layers with inclined elements displaying tensile buckling also holds for the analogous structure whose deformation is linked to compressive buckling.

3 Mechanics of the structure

The mechanics of the planar structure sketched in Fig. 1(a) and (b) is investigated. The system combines two superimposed articulated quadrilateral structures, made up of rigid bars connected to each other through hinges in a parallelogram shape, and equipped with a slider (imposing continuity of rotational and axial displacement, but allowing a jump in the transverse displacement) at the mid-span on the diagonal bars. The slider inside the j -th layer (two layers are considered, so that $j = 1, 2$) is activated when the related misalignment angle φ_j assumes a non-null value. After bifurcation, the kinematics of the j -th layer, maintaining the shape of a parallelogram (the horizontal bars are subject to pure translational motion), is described by the two angles α_j and β_j (configuration angles), both functions of φ_j as

$$\alpha_j(\varphi_j) = \arccos\left(\frac{\psi}{2\lambda \cos \varphi_j} + \chi \cos \varphi_j\right), \quad \beta_j(\varphi_j) = \arccos(\cos \beta_0 - \psi \tan^2 \varphi_j), \quad (21)$$

where λ and χ are constants depending on the initial configuration angles as follows

$$\lambda = \frac{\sin \beta_0}{2 \sin \alpha_0} > 0, \quad \chi = \frac{\sin(2\alpha_0 + \beta_0)}{\sin(\alpha_0 + \beta_0)}, \quad (22)$$

while ψ is as defined in eq. (5). Note that α_0 and β_0 correspond to α_j and β_j measured in the undeformed configuration described by $\varphi_j = 0$ and are subject to the geometrical constraints defined in eqs. (2) and (15).

The deformed state is subject to restoring forces provided by the linear elastic rotational springs of stiffness K_1 and K_2 , located at points indicated with letters ‘A’ and ‘B’, and unloaded in the undeformed configuration. The j -th layer is subject to the horizontal H_j and vertical V_j dead loads, acting at the middle of the horizontal upper bar. To simplify the presentation, the following dimensionless loads and the rotational stiffness ratios are introduced

$$h = \frac{H_1}{H_2}, \quad v = \frac{V_1}{V_2}, \quad k = \frac{K_1}{K_2} \geq 0. \quad (23)$$

From the above description, it follows that the system configuration is entirely described by the evolution of two degrees of freedom, namely, the misalignment angles φ_j ($j = 1, 2$). Due to the properties of the system and its similarities with a structure with a unilateral constraint shown in the previous Section, it is expedient to make reference to the difference angles $\theta_j = \beta_j - \beta_0$, evaluated for both layers similarly to eq. (4) as

$$\theta_j(\varphi_j) = -(-1)^j [\arccos(\cos \beta_0 - \psi \tan^2 \varphi_j) - \beta_0], \quad (24)$$

which yields the following constraints

$$\theta_1 \geq 0, \quad \theta_2 \leq 0, \quad \text{which imply} \quad \theta_1 \theta_2 \leq 0. \quad (25)$$

Finally, it is worth to highlight that the special case of the j -th parallelogram reducing to a line segment is provided by the following condition for the difference angle

$$|\theta_j| = \bar{\theta}^{[n]}, \quad \text{where} \quad \bar{\theta}^{[n]} = n\pi - \beta_0, \quad n \in \mathbb{N}, \quad (26)$$

implying that the misalignment angle φ_j is bounded as

$$|\varphi_j| \leq \bar{\varphi}, \quad \text{where} \quad \bar{\varphi} = \arctan \sqrt{\frac{1 + \cos \beta_0}{\psi}}. \quad (27)$$

4 Total potential energy and equilibrium

With reference to the misalignment angle φ_j , the total potential energy Π of the system sketched in panels (a) and (d) of Fig. 1, is given as the summation of the elastic energy stored in the two elastic hinges and the negative of the work done by the forces acting on each layer

$$\Pi(\varphi_1, \varphi_2) = K_2 \sum_{j=1}^2 \left\{ \frac{k^{2-j} [\theta_j(\varphi_j)]^2}{2} + (1+v)^{2-j} \mathcal{V} [\sin \beta_0 - \sin (\beta_0 - (-1)^j \theta_j(\varphi_j))] \right. \\ \left. + (-1)^j (1+h)^{2-j} \mathcal{H} [\cos \beta_0 - \cos (\beta_0 - (-1)^j \theta_j(\varphi_j))] \right\}, \quad (28)$$

where k , h and v are the stiffness and loading ratios defined in eq. (23), while \mathcal{H} and \mathcal{V} are the dimensionless horizontal and vertical dead loads acting on the upper layer, defined as

$$\mathcal{H} = \frac{H_2 l}{K_2}, \quad \mathcal{V} = \frac{V_2 l}{K_2}. \quad (29)$$

Further, the system of equilibrium equations can be obtained through the vanishing of the gradient of Π , eq. (28), with respect to the misalignment angles φ_j ,

$$\frac{\partial \Pi(\varphi_1, \varphi_2)}{\partial \varphi_j} = 0, \quad (30)$$

which through the chain rule of differentiation simplifies as

$$\frac{\partial \Pi(\theta_1, \theta_2)}{\partial \theta_1} \frac{\partial \theta_1}{\partial \varphi_j} + \frac{\partial \Pi(\theta_1, \theta_2)}{\partial \theta_2} \frac{\partial \theta_2}{\partial \varphi_j} = 0. \quad (31)$$

Considering eq. (24) the following property holds for the structure

$$\frac{\partial \theta_q}{\partial \varphi_j} = \begin{cases} 0, & q \neq j, \\ -(-1)^j \frac{2 \psi \tan \varphi_j}{\cos^2 \varphi_j \sqrt{1 - (\cos \beta_0 - \psi \tan^2 \varphi_j)^2}}, & q = j, \end{cases} \quad (32)$$

and therefore the equilibrium equation (30) is reduced to

$$\frac{\partial \Pi(\theta_1, \theta_2)}{\partial \theta_j} \frac{\partial \theta_j}{\partial \varphi_j} = 0, \quad (33)$$

where a repeated index does not imply summation, here and henceforth. The equilibrium equations (33) are always satisfied for the trivial configuration $\varphi_j = \theta_j = 0$ because

$$\left. \frac{\partial \theta_j}{\partial \varphi_j} \right|_{\varphi_j=0} = 0. \quad (34)$$

For non-trivial configurations, the equilibrium equations (33) in terms of the misalignment angle φ_j are quite complex, and therefore are not reported because impractical. However, making use of the equivalence between the two elementary structures reported in Fig. 3, it is expedient to write the

equilibrium conditions of the structure in a non-trivial configuration by utilizing as a parameter the difference angle $\theta_j \neq 0$ through

$$\frac{\partial \Pi(\theta_1, \theta_2)}{\partial \theta_j} = 0, \quad (35)$$

providing

$$\begin{aligned} (h+1)\mathcal{H} \sin(\beta_0 + \theta_1) + (v+1)\mathcal{V} \cos(\beta_0 + \theta_1) &= k \theta_1, & \text{for } \theta_1 > 0, \\ \mathcal{H} \sin(\beta_0 - \theta_2) - \mathcal{V} \cos(\beta_0 - \theta_2) &= \theta_2, & \text{for } \theta_2 < 0. \end{aligned} \quad (36)$$

Similarly to the simple case explained in Section 2, the difference angles θ_j do not represent Lagrangian parameters for the two-layer unit structure shown in Fig. 1 and therefore $\theta_j = 0$ is not a solution for the system of equations (36). In terms of the unilateral constraint model, when one or both of the layers composing the planar structure remain undeformed, a reaction emerges preventing the mechanism to move towards the constrained direction, but does not pose any obstacle to the opposite movement ($\theta_1 \geq 0$ and $\theta_2 \leq 0$). The unilateral constraints impose the following Kuhn-Tucker conditions

$$\begin{aligned} \theta_1 &\geq 0, & \mathcal{R}_1 &\geq 0, & \theta_1 \mathcal{R}_1 &= 0, \\ \theta_2 &\leq 0, & \mathcal{R}_2 &\leq 0, & \theta_2 \mathcal{R}_2 &= 0, \end{aligned} \quad (37)$$

where \mathcal{R}_1 and \mathcal{R}_2 are the reactions emerging in the constraint present within the respective layers, and are equivalent to the compression force in the bars with the slider. It is also interesting to note that equilibrium equations (36) reveal that the 2 degrees of freedom of the structure are decoupled. This implies that *the equilibrium of the two layers relies on the independent ‘individual’ equilibrium of each layer*. Therefore, depending on the existence of the non-trivial configuration for each layer, the equilibrium configurations for the entire structure can be distinguished in:

- trivial configuration ($\theta_1 = \theta_2 = 0$, always existing);
- non-trivial configuration for only the lower ($\theta_1 = 0$ and $\theta_2 < 0$) or the upper ($\theta_1 > 0$ and $\theta_2 = 0$) layer;
- non-trivial configuration for both layers ($\theta_1 > 0$ and $\theta_2 < 0$).

Non-trivial configurations are investigated in the next Section, along with the bifurcation conditions and the stability of equilibrium.

5 Bifurcation, equilibrium, and multistability

Bifurcation, post-critical behaviour, and stability of the two-layer unit structure shown in Fig. 1 are analyzed at varying dimensionless horizontal \mathcal{H} and vertical \mathcal{V} dead loads.

5.1 Critical loads and post-critical response

As mentioned, the equilibrium equations (31) are satisfied by the trivial configuration ($\varphi_j = \theta_j = 0$), while for the non-trivial configuration ($\varphi_j \neq 0$) reference can be made to the equilibrium condition expressed in terms of θ_j , eq. (36).

The linearized version of the equilibrium equations (36) can be obtained through a Taylor series expansion about $\theta_j = 0$ as

$$\begin{aligned} (h+1)\mathcal{H} \sin \beta_0 + (v+1)\mathcal{V} \cos \beta_0 &= \left(k + \frac{(v+1)\mathcal{V}}{\sin \beta_0} \right) \theta_1, & \text{for } \theta_1 > 0, \\ \mathcal{H} \sin \beta_0 - \mathcal{V} \cos \beta_0 &= \left(1 + \frac{\mathcal{V}}{\sin \beta_0} \right) \theta_2, & \text{for } \theta_2 < 0. \end{aligned} \quad (38)$$

The load pairs \mathcal{H} and \mathcal{V} , solution of eq. (38) at vanishing θ_j , represent the set of bifurcation conditions for the j -th layer, namely, the *critical load combinations*. The critical pair of loads corresponds to

$$\begin{cases} h+1 \\ 1 \end{cases} \mathcal{H}_{cr} \sin \beta_0 + \begin{cases} v+1 \\ -1 \end{cases} \mathcal{V}_{cr} \cos \beta_0 = 0, \quad \begin{array}{l} \text{for lower layer bifurcation,} \\ \text{for upper layer bifurcation,} \end{array} \quad (39)$$

showing independence of the stiffness of the rotational springs, so that *the system bifurcation is purely geometrical and only involves the referencial configuration angle β_0* .

From eq. (39), the following skew-symmetric behaviour is displayed

$$\mathcal{H}_{cr}(\mathcal{V}_{cr}, \beta_0) = -\mathcal{H}_{cr}(\mathcal{V}_{cr}, \pi - \beta_0), \quad (40)$$

and the simultaneous bifurcation of both layers occurs when

$$h + v = -2. \quad (41)$$

The post-buckling behaviour in terms of the difference angles θ_1 and θ_2 as functions of \mathcal{V} and \mathcal{H} , obtained as the solution of the nonlinear eqs. (36), is depicted in Fig. 4 (in the limited range $|\theta_j| < \pi - \beta_0$) for the six sets of parameters reported in Table 1, the first four associated to a non-symmetric response, while the last two correspond to a symmetric one.

Table 1: Sets of structural parameters corresponding to the equilibrium configurations reported in Fig. 4.

Panel	β_0	h	v	k	Panel	β_0	h	v	k
(a)	60°	-2.5	0.5	2	(d)	20°	1.5	3	3
(b)	20°	-2	0	3	(e)	120°	0	0	1
(c)	60°	0	1	1	(f)	80°	0	0	1

A total of three equilibrium surfaces is shown: the trivial equilibrium plane ($\theta_1 = \theta_2 = 0$) and two equilibrium surfaces corresponding to the non-trivial configuration for the lower ($\theta_1 > 0$) and the upper layer ($\theta_2 < 0$). The stability character (addressed in Section 5.2) of the portions of these equilibrium surfaces is also indicated with the letter ‘U_j’ or ‘S_j’, respectively denoting the ‘unstable’ or ‘stable’ configuration for the j -th layer (namely, U₁ defines an unstable configuration for the lower layer).

Fig. 4 can be interpreted in the following way: (stable or unstable) equilibrium configurations for θ_1 and θ_2 correspond to the intersections of the equilibrium surfaces with the (vertical dashed) line, defined by constant values of \mathcal{H} and \mathcal{V} , representing a load combination applied to the structure. Every vertical dashed line always intersects the trivial equilibrium surface, while depending on the structural

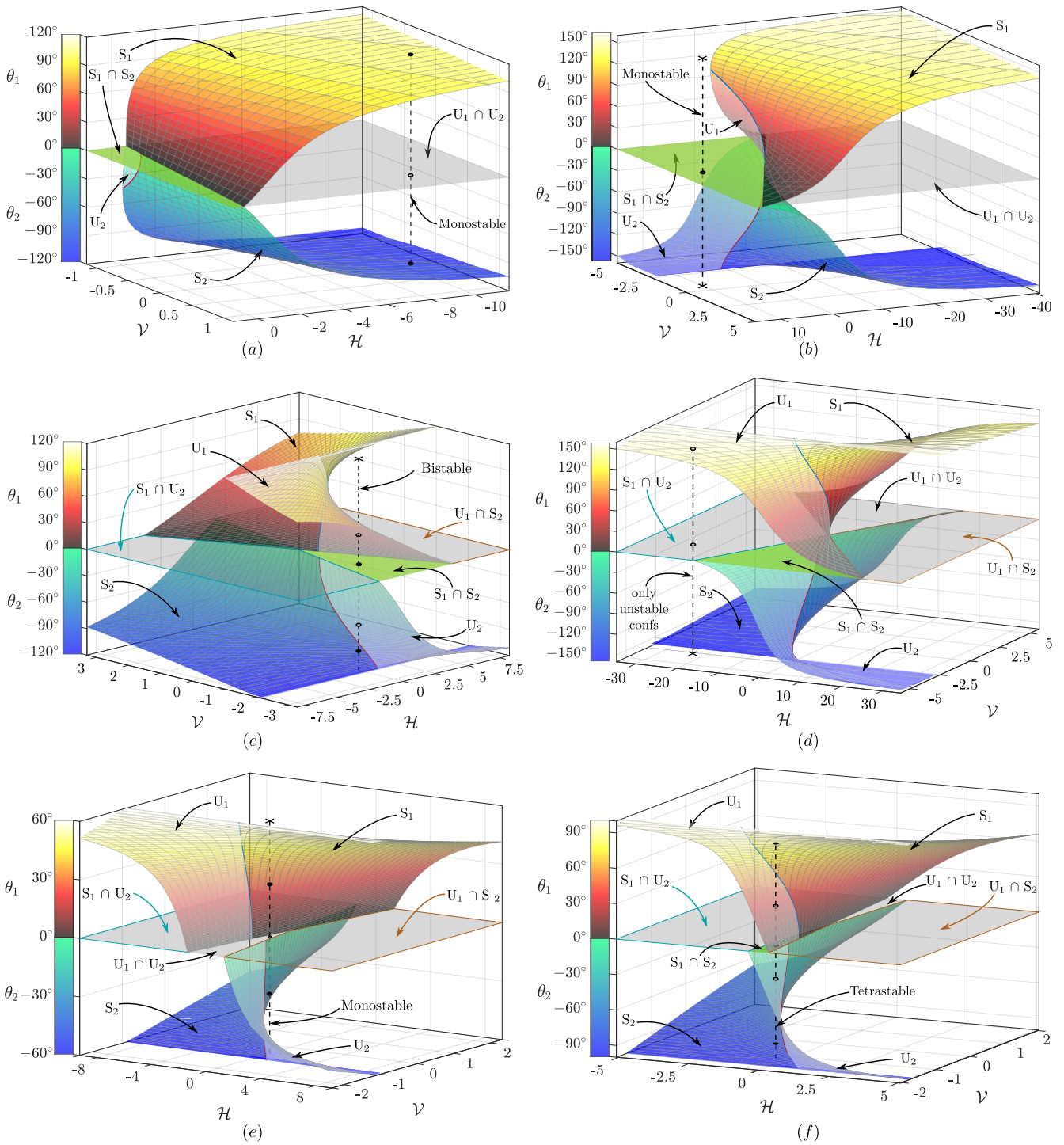


Figure 4: Equilibrium configurations in the \mathcal{H} - ν - θ_j space for the system described by the parameters sets (a)–(f) reported in Table 1. Stable and unstable configurations for the j -th layer are identified through the letters ‘ U_j ’ or ‘ S_j ’. Bifurcation loads \mathcal{H}_{cr} - ν_{cr} are given by the intersection of the non-trivial configuration surfaces with the trivial configuration plane ($\theta_j = 0$). Uniqueness, non-uniqueness, absence of stable configurations, monostability, bistability and tetrastability (within the limited range $|\theta_j| < \pi - \beta_0$ and) associated to specific loads combinations \mathcal{H} - ν (vertical dashed lines) are highlighted.

and loading parameters it may intersect none, one, or multiple times (in the considered difference angle range) the non-trivial surfaces.

Thus, with reference to the systems reported in Fig. 4, examples of loads combination show different numbers of intersections and consequently of equilibrium states. More specifically:

- for the load combination highlighted in Fig. 4(a) and (e), the vertical dashed line intersects 3 times the equilibrium surfaces, which correspond to four possible equilibrium configurations: (i.) $\theta_1 > 0$ and $\theta_2 < 0$, (ii.) $\theta_1 = 0$ and $\theta_2 < 0$, (iii.) $\theta_1 > 0$ and $\theta_2 = 0$ and finally (iv.) $\theta_1 = \theta_2 = 0$. Among these, only (i.) is stable, which corresponds to a deformation involving both layers;
- for the load combination highlighted in Fig. 4(b), the vertical dashed line intersects only the trivial equilibrium surface, corresponding to the stable trivial configuration for both layers;
- for the load combination highlighted in Fig. 4(c), the vertical dashed line intersects 4 times the equilibrium surfaces, leading to 6 equilibrium configurations: (i.) two sets of $\theta_1 > 0$ and $\theta_2 < 0$, (ii.) two sets of $\theta_1 = 0$ and $\theta_2 < 0$, (iii.) $\theta_1 > 0$ and $\theta_2 = 0$, and (iv.) the trivial state $\theta_1 = \theta_2 = 0$. Among these, only 2 configurations are stable: one of the sets in (ii.) and the trivial configuration (iv.), so that the system is *bistable* under the highlighted \mathcal{H} – \mathcal{V} loads combination;
- for the load combination highlighted in Fig. 4(d), the vertical dashed line intersects 2 times the equilibrium surfaces and 2 equilibrium configurations exist: (i.) $\theta_1 > 0$ and $\theta_2 = 0$ and (ii.) $\theta_1 = \theta_2 = 0$. Among these, none is stable;
- for the load combination highlighted in Fig. 4(f), the vertical dashed line intersects 5 times the equilibrium surfaces, providing a total of 9 different equilibrium configurations: (i.) four sets of $\theta_1 > 0$ and $\theta_2 < 0$, (ii.) two sets of $\theta_1 = 0$ and $\theta_2 < 0$, (iii.) two sets of $\theta_1 > 0$ and $\theta_2 = 0$ and (iv.) the trivial state $\theta_1 = \theta_2 = 0$. Among these, 4 configurations are stable: one per each of the sets (i.), (ii.), (iii.) and the trivial configuration (iv.), so that the system is *tetrastable* under the highlighted \mathcal{H} – \mathcal{V} load combination.

The non-uniqueness of equilibrium configurations (restricted to $|\theta_j| < \pi - \beta_0$) reported in Fig. 4(f) can be further appreciated through their projection onto the \mathcal{H} – \mathcal{V} plane, as reported in Fig. 5(a). The influence of the angle β_0 is shown through the complementary projections corresponding to $\beta_0 = 90^\circ$, Fig. 5(b), and to $\beta_0 = 100^\circ$, Fig. 5(c), with the other structural and loading parameters remaining the same as in Fig. 5(a).

A total of nine regions for \mathcal{H} – \mathcal{V} load combinations are distinguished, corresponding to a different number and type of equilibrium configurations. The corresponding stable configurations are sketched for each region visible in Fig. 5(a). The properties of the equilibrium configurations of these nine regions are summarized in Table 2, showing that, when the load combination \mathcal{H} – \mathcal{V} varies, under the restriction $|\theta_j| < \pi - \beta_0$, the system changes the number of its stable equilibrium configurations and in particular can display: none (regions O' and F), one (*monostable*, regions O, C, D, and E), two (*bistable*, regions A and G), or four (*tetrastable*, region B) stable equilibrium configurations.

It can be observed that the number of stable configurations can be reduced by increasing the angle β_0 , for example the *tetrastability* region disappears, while the region without stable equilibrium solutions expands. Moreover, roughly speaking, the monostable region O is mirrored around the \mathcal{H} –axis, when β_0 moves from the range $(0, 90^\circ)$ to the range $(90^\circ, 180^\circ)$. It is also interesting to note that the system may turn from *monostable* to *tetrastable* without displaying an intermediate *bistable* behaviour, as in the case reported in Fig. 5(a) by decreasing values of \mathcal{V} at $\mathcal{H} = 0$.

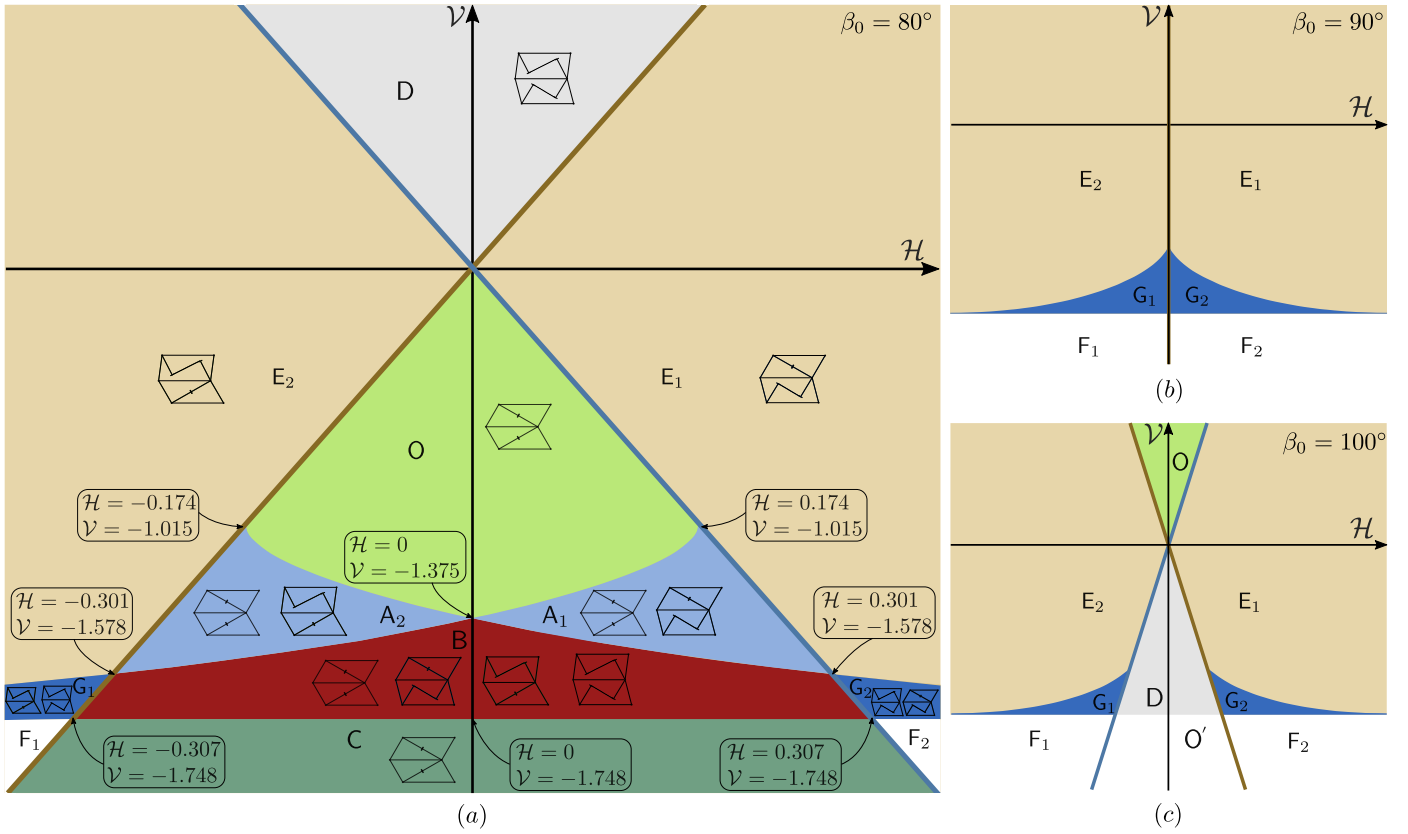


Figure 5: (a) Projection onto the $\mathcal{H} - \mathcal{V}$ plane of the equilibrium surfaces (limited to $|\theta_j| < \pi - \beta_0$) reported in Fig. 4(f), corresponding to the parameters set (f) of Table 1. Stable equilibrium configurations are sketched inside each region, except for regions F_j , where stable configuration do not exist. Regions with the same letter, but differing because the j -th layer displays a non-trivial configuration, are distinguished through the subscript j . Panels (b) and (c) are as panels (a), except that $\beta_0 = 90^\circ$ and $\beta_0 = 100^\circ$, respectively. The number and properties of the equilibrium configurations corresponding to the different nine regions are listed in Table 2.

To further appreciate the generation of more than one stable configurations, the contourplots of the total potential energy Π , eq. (28), on the difference angles plane $\theta_1 - \theta_2$ are reported in Fig. 6 for the parameters set (f) of Table 1. The contourplots for six different pairs of $\mathcal{H} - \mathcal{V}$ loads show how the number of total potential energy wells changes, defining (a, c, d, e) *monostable*, (f) *bistable*, or (b) *tetrastable* systems.

Equilibrium configurations expressed as horizontal \mathcal{H} and the vertical \mathcal{V} loads, functions of the difference angles θ_1 and θ_2 are reported in Fig. 7, at fixed values of the remaining parameters. Stable and unstable configurations are distinguished through continuous and dashed lines. The reported curves show how significantly the different parameters affect the critical loads, the post-buckling response of the structure (by turning the incremental stiffness from positive to negative and by realizing force-reversal conditions), and the stability. More specifically,

- bifurcation of both layers occurs at the unloaded state ($\mathcal{H} = \mathcal{V} = 0$), Fig. 7(a, b);
- at constant vertical load \mathcal{V} , the bifurcation load \mathcal{H}_{cr} and the post-buckling behaviour can be tuned also by varying the configuration angle β_0 , Fig. 7(c);

Table 2: Number of the equilibrium configurations and their stability corresponding to the regions of load combination \mathcal{H} – \mathcal{V} reported in Fig. 5.

label	stable trivial configuration	# non-trivial configurations	# stable non-trivial configurations	structural response
O'	no	0	0	only unstable confs
O	yes	0	0	<i>monostable</i>
A	yes	2	1	<i>bistable</i>
B	yes	8	3	<i>tetrastable</i>
C	yes	3	0	<i>monostable</i>
D	no	3	1	<i>monostable</i>
E	no	1	1	<i>monostable</i>
F	no	1	0	only unstable confs
G	no	5	2	<i>bistable</i>

- when the deformed j -th layer assumes the rectangular shape, condition occurring for $\theta_j = -(-1)^j(\pi/2 - \beta_0)$, the following situations occur:

– the equilibrium is independent of the vertical loads (\mathcal{V} and v), Fig. 7(a), when

$$\begin{aligned} \mathcal{H} &= \left(\frac{\pi}{2} - \beta_0\right) \frac{k}{(h+1)}, \quad \forall \mathcal{V} \text{ and } v \quad \text{for } \theta_1 = \frac{\pi}{2} - \beta_0, \\ \mathcal{H} &= -\left(\frac{\pi}{2} - \beta_0\right), \quad \forall \mathcal{V} \text{ and } v \quad \text{for } \theta_2 = -\frac{\pi}{2} + \beta_0; \end{aligned} \quad (42)$$

– when the horizontal force \mathcal{H} does not satisfy eq. (42), the rectangular configuration is attained only at an infinite value of the vertical load \mathcal{V} , Fig. 7(b, f), representing a *locking condition* for the system;

- when $h < 0$, a stable (an unstable) post-critical behaviour can be associated to negative (positive) slope in the equilibrium path $\mathcal{H} - \theta_j$, Fig. 7(a, e);
- when $\mathcal{H} = 0$, the equilibrium angle θ_1 is independent of h , Fig. 7(e);
- the stiffness and loading ratios k , h and v influence the bifurcation load and the post-critical behaviour of the lower layer only, Fig. 7(d, e, f);
- at null horizontal load ($\mathcal{H} = 0$), both layers bifurcate simultaneously when the vertical load \mathcal{V} is greater than zero for $\beta_0 \in (0, \pi/2)$, Fig. 7(b), or is smaller than zero for $\beta_0 \in (\pi/2, \pi)$.

Symmetric response. When the stiffness ratio k and the loading ratios h and v satisfy the following condition

$$k = v + 1 = h + 1, \quad (43)$$

the post-critical response defined by eq. (36) reduces to

$$-(-1)^j \mathcal{H} \sin(\beta_0 + |\theta_j|) + \mathcal{V} \cos(\beta_0 + |\theta_j|) = |\theta_j|, \quad (44)$$

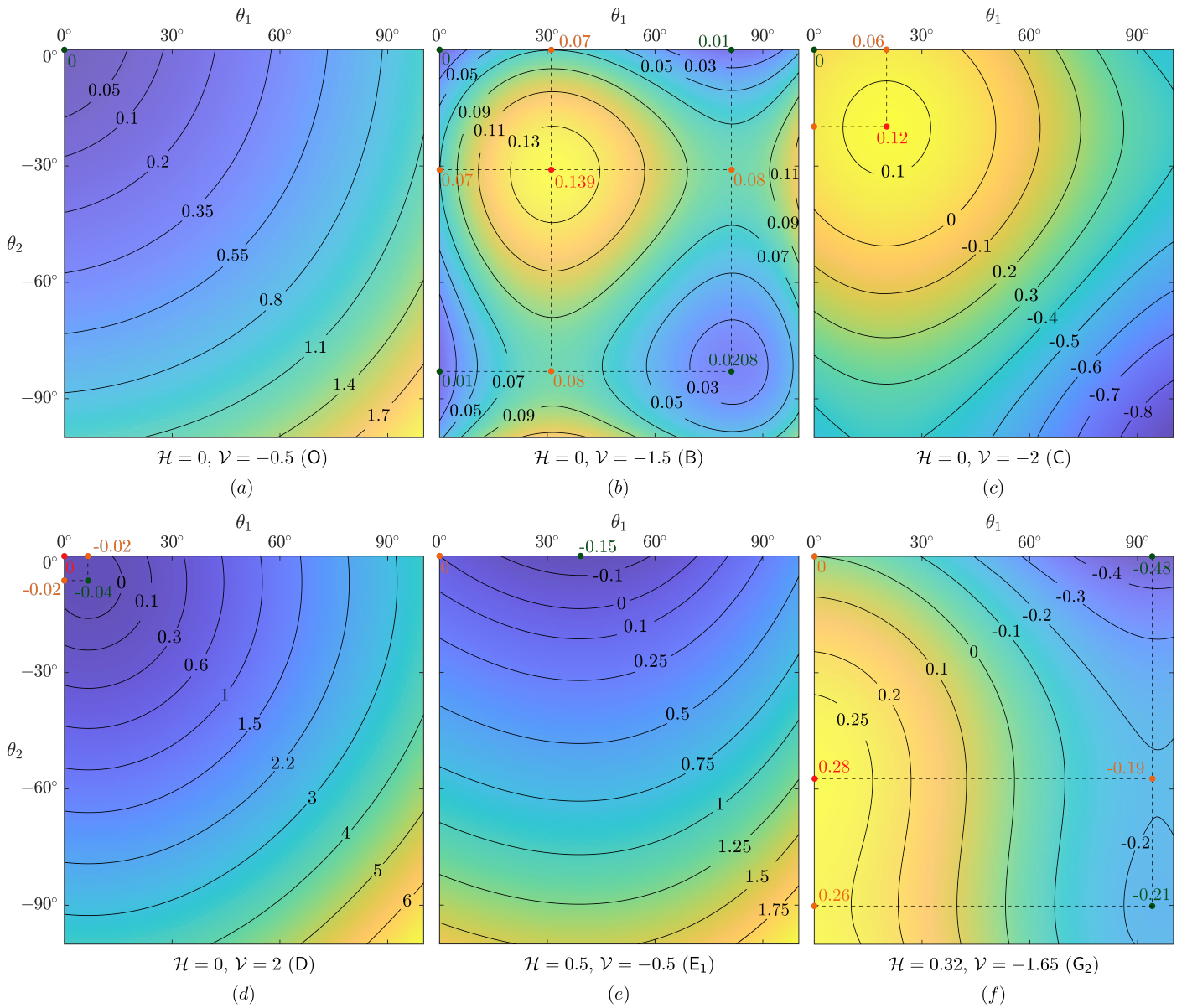


Figure 6: Contourplots of the dimensionless total potential energy Π/K_2 , eq. (28), on the difference angles plane θ_1 - θ_2 for a system defined by the parameters set (f) of Table 1 and for six different pairs of loads $\mathcal{H} - \nu$. By varying the applied loads, the number of total potential energy wells changes, defining a (a, c, d, e) *monostable*, (f) *bistable*, and (b) *tetrastable* system. Green, red, and orange circles respectively define local minima, local maxima, and saddle points, and therefore the first correspond to stable equilibrium configurations, while the second and third to unstable ones.

which implies the following symmetry property

$$\theta_1(\mathcal{H}, \nu) = -\theta_2(-\mathcal{H}, \nu). \quad (45)$$

It is finally noted that, due the positiveness of k , the condition (43), defining the symmetric response (45), may be realized only when

$$h > -1 \quad \text{and} \quad v > -1, \quad (46)$$

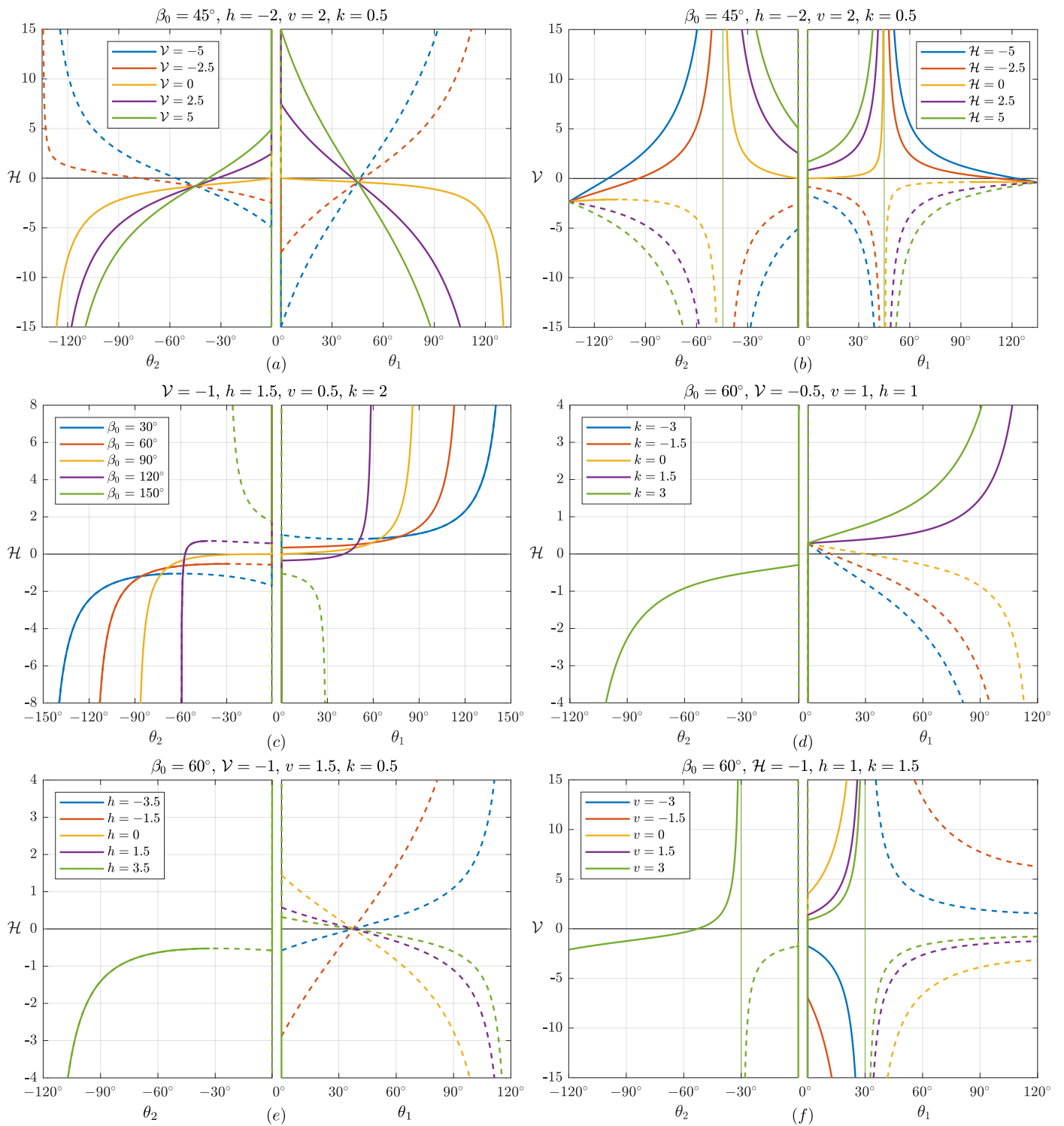


Figure 7: Equilibrium configurations in terms of difference angles θ_1 and θ_2 versus the load \mathcal{H} or \mathcal{V} at fixed value of the remaining parameters (\mathcal{V} or \mathcal{H} , h , v , k , and β_0) as specified in each panel. Stable and unstable configurations are displayed as continuous and dashed curves, respectively.

which includes the particular case of rotational springs of equal stiffness and absence of forces acting

on the top of the lower layer,

$$h = 0, \quad v = 0, \quad k = 1. \quad (47)$$

5.2 Stability of the equilibrium

According to the Dirichlet criterion, stability corresponds to the positive definiteness of the Hessian (symmetric) matrix \mathbb{H} of the total potential energy Π , whose components are given by

$$\mathbb{H}_{ij} = \sum_{q=1}^2 \sum_{r=1}^2 \left(\frac{\partial^2 \Pi}{\partial \theta_q \partial \theta_r} \frac{\partial \theta_q}{\partial \varphi_j} \frac{\partial \theta_r}{\partial \varphi_i} + \frac{\partial \Pi}{\partial \theta_q} \frac{\partial^2 \theta_q}{\partial \varphi_j \partial \varphi_i} \right). \quad (48)$$

Considering the total potential energy Π expressed by eq. (28) and the property in eq. (32), the following conditions holds

$$\frac{\partial^2 \Pi}{\partial \theta_i \partial \theta_j} = 0, \quad i \neq j. \quad (49)$$

Therefore, the Hessian matrix is diagonal ($\mathbb{H}_{12} = \mathbb{H}_{21} = 0$) and its eigenvalues μ_j coincide with the corresponding diagonal terms,

$$\mu_j = \mathbb{H}_{jj} = \frac{\partial^2 \Pi}{\partial \theta_j^2} \left(\frac{\partial \theta_j}{\partial \varphi_j} \right)^2 + \frac{\partial \Pi}{\partial \theta_j} \frac{\partial^2 \theta_j}{\partial \varphi_j^2}, \quad (50)$$

where

$$\frac{\partial^2 \theta_j}{\partial \varphi_j^2} = -(-1)^j \frac{2 \psi \left[\frac{\sin^2 \beta_0 + \psi^2 \tan^4 \varphi_j}{\cos^2 \varphi_j} + 2 \tan^2 \varphi_j \left(1 - (\cos \beta_0 - \psi \tan^2 \varphi_j)^2 \right) \right]}{\cos^2 \varphi_j \sqrt{\left[1 - (\cos \beta_0 - \psi \tan^2 \varphi_j)^2 \right]^3}}. \quad (51)$$

It is interesting to note that each eigenvalue only depends on the respective difference angle, namely

$$\mu_j = \mu_j(\theta_j), \quad (52)$$

and therefore, as for the equilibrium, the stability analysis of the equilibrium configuration is decoupled for the two layers. Considering that the conditions of stability, called ‘S_j’, and instability, called ‘U_j’, of the equilibrium configuration θ_j for the j -th layer are given by

$$\left. \begin{array}{l} S_j \\ U_j \end{array} \right\} : \text{sgn}[\mu_j(\theta_j)] \left\{ \begin{array}{l} > 0, \quad \text{Stable} \\ < 0, \quad \text{Unstable} \end{array} \right\} \text{ configuration for the } j\text{-th layer}, \quad (53)$$

it follows that *the stability of the equilibrium configuration for the two-layer unit structure is provided by the simultaneous ‘individual’ stability of the configuration assumed by each layer, corresponding to $S_1 \cap S_2$.*

Considering all of the above, the stability of the trivial and non-trivial configurations is addressed separately.

Trivial configuration. When $\theta_j = 0$, the first and second derivatives of the difference angle θ_j with respect to the misalignment angle φ_j , eqs. (32) and (51), reduce to

$$\frac{\partial \theta_j}{\partial \varphi_j} = 0, \quad \frac{\partial^2 \theta_j}{\partial \varphi_j^2} = -(-1)^j \frac{2 \psi}{\sin \beta_0}, \quad (54)$$

and the eigenvalues become

$$\mu_j = \frac{\partial \Pi}{\partial \theta_j} \frac{\partial^2 \theta_j}{\partial \varphi_j^2}. \quad (55)$$

Therefore, from eq. (55) the stability conditions (53) for the trivial equilibrium path read as

$$\left. \begin{array}{l} S_1 \\ U_1 \end{array} \right\} : (h+1)\mathcal{H} \sin \beta_0 + (v+1)\mathcal{V} \cos \beta_0 \left\{ \begin{array}{l} < 0, & \text{Stable} \\ > 0, & \text{Unstable} \end{array} \right\} \begin{array}{l} \text{trivial configuration} \\ \text{of the lower layer,} \end{array} \quad (56)$$

$$\left. \begin{array}{l} S_2 \\ U_2 \end{array} \right\} : \mathcal{H} \sin \beta_0 - \mathcal{V} \cos \beta_0 \left\{ \begin{array}{l} > 0, & \text{Stable} \\ < 0, & \text{Unstable} \end{array} \right\} \text{trivial configuration of the upper layer,}$$

which is used to define the stable or unstable character of the trivial equilibrium configuration $\theta_j = 0$ displayed in Figs. 2, 4, 5, 7. As a consequence, the trivial configuration of the two-layer unit structure is stable when

$$S_1 \cap S_2 : (h+1)\mathcal{H} \sin \beta_0 + (v+1)\mathcal{V} \cos \beta_0 < 0, \quad \mathcal{H} \sin \beta_0 - \mathcal{V} \cos \beta_0 > 0. \quad (57)$$

Four regions of loading combinations \mathcal{H} – \mathcal{V} can be distinguished according to the stability of the trivial configuration assumed by the two layers, and corresponding to the following situations: (i.) stable undeformed configuration for both layers ($S_1 \cap S_2$); (ii.) unstable undeformed configuration for both layers ($U_1 \cap U_2$); (iii.) unstable undeformed configuration for the lower layer and stable for the upper one ($U_1 \cap S_2$); (iv.) unstable undeformed configuration for the upper layer and stable for the lower ($S_1 \cap U_2$).

Finally, it is interesting to note that the stability condition (57) reduces in the case of rectangular undeformed layers ($\beta_0 = \pi/2$) to

$$S_1 \cap S_2 : \mathcal{H} > 0, \quad h < -1, \quad \forall \mathcal{V}. \quad (58)$$

Non-trivial configuration. When $\theta_j \neq 0$, the equilibrium condition reduces to

$$\frac{\partial \Pi}{\partial \theta_j} = 0, \quad (59)$$

therefore the j -th eigenvalue simplifies to

$$\mu_j = \frac{\partial^2 \Pi}{\partial \theta_j^2} \left(\frac{\partial \theta_j}{\partial \varphi_j} \right)^2, \quad (60)$$

and its sign coincides with that of the second derivative of the total potential energy,

$$\text{sgn} [\mu_j] = \text{sgn} \left[\frac{\partial^2 \Pi}{\partial \theta_j^2} \right]. \quad (61)$$

The sign of the second derivative of the total potential energy with respect to θ_j defines the stable or unstable character of the non-trivial equilibrium configuration for the difference angle θ_j , as displayed in Figs. 2, 4, 5, 7. Due to the high nonlinearities, the second derivative of the total potential energy, evaluated at the non-trivial equilibrium configuration, is given by a complicated expression and therefore is omitted. However, a first-order expansion in the difference angle amplitude allows to evaluate this quantity through the following expression

$$\left. \frac{\partial^2 \Pi}{\partial \theta_j^2} \right|_{\mathcal{H}=\mathcal{H}(\theta_j, \mathcal{V})} = \left(k^{2-j} + \frac{(v+1)^{2-j} \mathcal{V}}{\sin \beta_0} \right) \left(1 - \frac{|\theta_j|}{\tan \beta_0} \right), \quad (62)$$

and the stability conditions (53) reduce for small difference angles ($|\theta_j| \gg \theta_j^2$) to

$$\left. \begin{array}{l} S_1 \\ U_1 \end{array} \right\} : k + \frac{(v+1) \mathcal{V}}{\sin \beta_0} \left\{ \begin{array}{l} > 0, \text{ Stable} \\ < 0, \text{ Unstable} \end{array} \right\} \text{non-trivial configuration for the lower layer,} \quad (63)$$

$$\left. \begin{array}{l} S_2 \\ U_2 \end{array} \right\} : 1 + \frac{\mathcal{V}}{\sin \beta_0} \left\{ \begin{array}{l} > 0, \text{ Stable} \\ < 0, \text{ Unstable} \end{array} \right\} \text{non-trivial configuration for the upper layer,}$$

showing that just after the bifurcation, the stability of the non-trivial path is affected also by the stiffness ratio k and the load ratios h and v , in addition to the angle β_0 .

6 Conclusions

The nonlinear quasi-static mechanical behaviour of a structural element, to be used as a unit structure for metamaterial design, has been analyzed. The structural element exhibits a complex bifurcation landscape, with multiple (stable and unstable) equilibrium configurations as related to the presence of an element susceptible to buckling at vanishing load under tension or compression. This element introduces a mechanical equivalence with a unilateral constraint, thus strongly conditioning dynamics, which will be analyzed elsewhere.

Authors' Contributions. The presented structure was designed and developed by all authors. They also cooperated in the development of calculations and in the writing of the paper. In addition, NH created all the codes for symbolic manipulation and numerical results. He also prepared all the figures.

Acknowledgments. NH and FDC gratefully acknowledge the financial support from the European Union's Horizon 2020 research and innovation programme under the Marie Skłodowska-Curie grant agreement 'INSPIRE - Innovative ground interface concepts for structure protection' PITN-GA-2019-813424-INSPIRE. DB gratefully acknowledges financial support from the ERC advanced grant ERC-2021-AdG-101052956-BEYOND. Support from the Italian Ministry of Education, University and Research (MIUR) in the frame of the 'Departments of Excellence' grant L. 232/2016 is acknowledged. This work has been developed under the auspices of INDAM-GNFM.

References

- [1] X. Guo, V. E. Gusev, K. Bertoldi, and V. Tournat, “Manipulating acoustic wave reflection by a nonlinear elastic metasurface,” *J. Appl. Phys.*, vol. 123, p. 124901, mar 2018.
- [2] K. Bertoldi, V. Vitelli, J. Christensen, and M. van Hecke, “Flexible mechanical metamaterials,” *Nat. Rev. Mater.*, vol. 2, no. 11, p. 17066, 2017.
- [3] G. Carta, M. Brun, and A. Baldi, “Design of a porous material with isotropic negative Poisson’s ratio,” *Mech. Mater.*, vol. 97, pp. 67–75, 2016.
- [4] G. Carta, M. J. Nieves, I. S. Jones, N. V. Movchan, and A. B. Movchan, “Elastic Chiral Waveguides with Gyro-Hinges,” *Q. J. Mech. Appl. Math.*, vol. 71, pp. 157–185, may 2018.
- [5] L. D’Alessandro, E. Belloni, R. Ardito, A. Corigliano, and F. Braghin, “Modeling and experimental verification of an ultra-wide bandgap in 3D phononic crystal,” *Appl. Phys. Lett.*, vol. 109, p. 221907, nov 2016.
- [6] S. D. M. Adams, R. V. Craster, and S. Guenneau, “Bloch waves in periodic multi-layered acoustic waveguides,” *Proc. R. Soc. A Math. Phys. Eng. Sci.*, vol. 464, pp. 2669–2692, oct 2008.
- [7] L. D’Alessandro, R. Ardito, F. Braghin, and A. Corigliano, “Low frequency 3D ultra-wide vibration attenuation via elastic metamaterial,” *Sci. Rep.*, vol. 9, no. 1, p. 8039, 2019.
- [8] M. Garau, G. Carta, M. J. Nieves, I. S. Jones, N. V. Movchan, and A. B. Movchan, “Interfacial waveforms in chiral lattices with gyroscopic spinners,” *Proc. R. Soc. A Math. Phys. Eng. Sci.*, vol. 474, p. 20180132, jul 2018.
- [9] S. G. Haslinger, N. V. Movchan, A. B. Movchan, I. S. Jones, and R. V. Craster, “Controlling Flexural Waves in Semi-Infinite Platonic Crystals with Resonator-Type Scatterers,” *Q. J. Mech. Appl. Math.*, vol. 70, pp. 216–247, aug 2017.
- [10] D. Misseroni, A. B. Movchan, and D. Bigoni, “Omnidirectional flexural invisibility of multiple interacting voids in vibrating elastic plates,” *Proc. R. Soc. A Math. Phys. Eng. Sci.*, vol. 475, p. 20190283, sep 2019.
- [11] A. Diatta and S. Guenneau, “Controlling solid elastic waves with spherical cloaks,” *Appl. Phys. Lett.*, vol. 105, p. 21901, jul 2014.
- [12] L. Cabras, A. B. Movchan, and A. Piccolroaz, “Floquet–Bloch Waves in Periodic Networks of Rayleigh Beams: Cellular System, Dispersion Degenerations, and Structured Connection Regions,” *Mech. Solids*, vol. 52, no. 5, pp. 549–563, 2017.
- [13] S. Babae, J. Overvelde, E. Chen, V. Tournat, and K. Bertoldi, “Reconfigurable origami-inspired acoustic waveguides,” *Sci. Adv.*, vol. 2, p. e1601019, nov 2016.
- [14] R. V. Craster and S. Guenneau, *Acoustic Metamaterials: Negative Refraction, Imaging, Lensing and Cloaking*. NL: Springer, 2012.
- [15] L. D’Alessandro, E. Belloni, R. Ardito, F. Braghin, and A. Corigliano, “Mechanical low-frequency filter via modes separation in 3D periodic structures,” *Appl. Phys. Lett.*, vol. 111, p. 231902, dec 2017.

- [16] G. W. Milton, M. Briane, and J. R. Willis, “On cloaking for elasticity and physical equations with a transformation invariant form,” *New J. Phys.*, vol. 8, no. 10, p. 248, 2006.
- [17] D. Misseroni, D. J. Colquitt, A. B. Movchan, N. V. Movchan, and I. S. Jones, “Cymatics for the cloaking of flexural vibrations in a structured plate,” *Sci. Rep.*, vol. 6, no. 1, p. 23929, 2016.
- [18] J. R. Willis, “Negative refraction in a laminate,” *J. Mech. Phys. Solids*, vol. 97, nov 2015.
- [19] T. Frenzel, M. Kadic, and M. Wegener, “Three-dimensional mechanical metamaterials with a twist,” *Science*, vol. 358, pp. 1072–1074, nov 2017.
- [20] X. Hou, H. Hu, and V. Silberschmidt, “Erratum to: A composite material with Poisson’s ratio tunable from positive to negative values: an experimental and numerical study,” *J. Mater. Sci.*, vol. 49, no. 1, p. 461, 2014.
- [21] M. Kadic, A. Diatta, T. Frenzel, S. Guenneau, and M. Wegener, “Static chiral Willis continuum mechanics for three-dimensional chiral mechanical metamaterials,” *Phys. Rev. B*, vol. 99, p. 214101, jun 2019.
- [22] M. Kadic, G. W. Milton, M. van Hecke, and M. Wegener, “3D metamaterials,” *Nat. Rev. Phys.*, vol. 1, no. 3, pp. 198–210, 2019.
- [23] K. Liu, L. S. Novelino, P. Gardoni, and G. H. Paulino, “Big influence of small random imperfections in origami-based metamaterials,” *Proc. R. Soc. A Math. Phys. Eng. Sci.*, vol. 476, p. 20200236, sep 2020.
- [24] Z. Lin, L. S. Novelino, H. Wei, N. A. Alderete, G. H. Paulino, H. D. Espinosa, and S. Krishnaswamy, “Folding at the Microscale: Enabling Multifunctional 3D Origami-Architected Metamaterials,” *Small*, vol. 16, p. e2002229, sep 2020.
- [25] Y. Ma, Q. Zhang, Y. Dobah, F. Scarpa, F. Fraternali, R. E. Skelton, D. Zhang, and J. Hong, “Meta-tensegrity: Design of a tensegrity prism with metal rubber,” *Compos. Struct.*, vol. 206, pp. 644–657, 2018.
- [26] A. Zinco, F. Fraternali, G. Benzoni, and E. Martinelli, “On the Distribution in Height of Base Shear Forces in Linear Static Analysis of Base-Isolated Structures,” *Buildings*, vol. 10, no. 11, 2020.
- [27] J. B. Berger, H. N. G. Wadley, and R. M. McMeeking, “Mechanical metamaterials at the theoretical limit of isotropic elastic stiffness,” *Nature*, vol. 543, no. 7646, pp. 533–537, 2017.
- [28] T. Bückmann, M. Thiel, M. Kadic, R. Schittny, and M. Wegener, “An elasto-mechanical unfeability cloak made of pentamode metamaterials,” *Nat. Commun.*, vol. 5, no. 1, p. 4130, 2014.
- [29] C. Coulais, C. Kettenis, and M. van Hecke, “A characteristic length scale causes anomalous size effects and boundary programmability in mechanical metamaterials,” *Nat. Phys.*, vol. 14, no. 1, pp. 40–44, 2018.
- [30] D. Mousanezhad, S. Babae, H. Ebrahimi, R. Ghosh, A. S. Hamouda, K. Bertoldi, and A. Vaziri, “Hierarchical honeycomb auxetic metamaterials,” *Sci. Rep.*, vol. 5, no. 1, p. 18306, 2015.

- [31] Q. Zhang, W. Lu, F. Scarpa, D. Barton, R. S. Lakes, Y. Zhu, Z. Lang, and H.-X. Peng, “Large stiffness thermoformed open cell foams with auxeticity,” sep 2020.
- [32] L. Cabras, M. Brun, and D. Misseroni, “Micro-structured medium with large isotropic negative thermal expansion,” *Proc. R. Soc. A Math. Phys. Eng. Sci.*, vol. 475, p. 20190468, dec 2019.
- [33] S. Shan, S. H. Kang, J. R. Raney, P. Wang, L. Fang, F. Candido, J. A. Lewis, and K. Bertoldi, “Multistable architected materials for trapping elastic strain energy,” *Advanced Materials*, vol. 27, no. 29, 2015.
- [34] N. Singh and M. van Hecke, “Design of pseudo-mechanisms and multistable units for mechanical metamaterials,” *Phys. Rev. Lett.*, vol. 126, Jun 2021.
- [35] R. Khajehtourian, M. J. Frazier, and D. M. Kochmann, “Multistable pendula as mechanical analogs of ferroelectricity,” *Extreme Mechanics Letters*, vol. 50, 2022.
- [36] L. Medina and A. A. Seshia, “Tristable properties and limit point behaviour in electrostatically actuated initially curved coupled micro beams,” *International Journal of Mechanical Sciences*, vol. 204, 2021.
- [37] Y. Yang, M. A. Dias, and D. P. Holmes, “Multistable kirigami for tunable architected materials,” *Phys. Rev. Materials*, vol. 2, Nov 2018.
- [38] P. M. Reis, “A Perspective on the Revival of Structural (In)Stability With Novel Opportunities for Function: From Buckliphobia to Buckliphilia,” *J. Appl. Mech.*, vol. 82, sep 2015.
- [39] D. Bigoni, *Extremely Deformable Structures*. Wien, AT: Springer, 2015.
- [40] D. Yang, B. Mosadegh, A. Ainla, B. Lee, F. Khashai, Z. Suo, K. Bertoldi, and G. M. Whitesides, “Buckling of Elastomeric Beams Enables Actuation of Soft Machines.,” *Adv. Mater.*, vol. 27, pp. 6323–6327, nov 2015.
- [41] D. Bigoni, F. Dal Corso, D. Misseroni, and F. Bosi, “Torsional locomotion,” *Proc. R. Soc. A Math. Phys. Eng. Sci.*, vol. 470, p. 20140599, nov 2014.
- [42] T. Chen, O. R. Bilal, K. Shea, and C. Daraio, “Harnessing bistability for directional propulsion of soft, untethered robots,” *Proc. Nat. Aca. Sci.*, vol. 115, no. 22, 2018.
- [43] F. Bosi, D. Misseroni, F. Dal Corso, and D. Bigoni, “An elastica arm scale,” *Proc. R. Soc. A Math. Phys. Eng. Sci.*, vol. 470, p. 20140232, sep 2014.
- [44] D. Zaccaria, D. Bigoni, G. Noselli, and D. Misseroni, “Structures buckling under tensile dead load,” *Proc. R. Soc. A Math. Phys. Eng. Sci.*, vol. 467, pp. 1686–1700, jun 2011.